Journal of Materials Chemistry A

PAPER

View Article Online
View Journal | View Issue

Cite this: J. Mater. Chem. A, 2014, 2, 2757

Real-time materials evolution visualized within intact cycling alkaline batteries

Joshua W. Gallaway,*[a] Can K. Erdonmez,*[b] Zhong Zhong,[c] Mark Croft,[cd] Lev A. Sviridov,[a] Tal Z. Sholklapper,[a] Damon E. Turney,[a] Sanjoy Banerjee[a] and Daniel A. Steingart*[ef]

Received 12th December 2013
Accepted 7th January 2014

DOI: 10.1039/c3ta15169g

www.rsc.org/MaterialsA

The scientific community has focused on the problem of inexpensive, safe, and sustainable large-scale electrical energy storage, which is needed for a number of emerging societal reasons such as stabilizing intermittent renewables-based generation like solar and wind power. The materials used for large-scale storage will need to be low cost, earth-abundant, and safe at the desired scale. The Zn–MnO_2 "alkaline" battery chemistry is associated with one-time use, despite being rechargeable. This is due to material irreversibilities that can be triggered in either the anode or cathode. However, as Zn and MnO_2 have high energy density and low cost, they are economically attractive even at limited depth of discharge. As received, a standard bobbin-type alkaline cell costs roughly $20 per kW h. The U.S. Department of Energy ARPA-E $100 per kW h cost target for grid storage is thus close to the cost of alkaline consumer primary cells if re-engineered and/or cycled at 5–20% nominal capacity. Herein we use a deeply-penetrating *in situ* technique to observe ZnO precipitation near the separator in an alkaline cell anode cycled at 5% DOD, which is consistent with cell failures observed at high cycle life. Alkaline cells designed to avoid such causes of cell failure could serve as a low-cost baseload for large-scale storage.

1. Introduction

The abundance and safety of zinc and electrolytic manganese dioxide (EMD) make the Zn–MnO_2 alkaline battery chemistry a good candidate for large-scale, stationary storage provided cycle life and round trip efficiency are sound. It is generally recognized that electrical storage at the grid scale is needed for a number of emerging societal reasons such as load leveling and stabilizing intermittent renewables-based generation.[1–3] A recent review has stated that "in the future, the preferred energy storage technologies will be composed of low cost, easily acquired materials that are developed into products through a relatively simple manufacturing process".[2] Zn and MnO_2 are earth-abundant, safe, and water compatible. Additionally, they have high energy density and low cost, and are thus economically attractive even at limited depth of discharge (DOD) as low as 5%. Thus alkaline cells can play a role in the radical transformation in battery deployment needed for societal-scale renewable energy.

During discharge of an alkaline battery, zinc is oxidized, releasing electrons and aqueous zincate ions. Manganese dioxide is reduced in the solid state, with a concomitant proton insertion into the crystal structure. Alkaline batteries are generally associated with one-time use, despite being rechargeable. This is due to cycling-induced material changes in the anode and cathode, both of which can cause failure depending on conditions and cell design.[4,5] The most frequently-cited is an irreversible lattice strain that over-cycling triggers in the MnO_2 cathode material.[6] Due to the non-uniform current distributions that prevail in well-designed, practical batteries this strain is highly localized within the cell. Energy dispersive X-ray diffraction (EDXRD) is a technique developed for strain depth-profiling in high performance materials using deeply penetrating, high-energy radiation.[7] EDXRD from a source with high spectral flux allows diffraction information to be collected rapidly within an intact battery through its steel containment, at small, well-defined spatial locations. This allowed visualization of the local strain in LR20 (D cell) batteries in real-time during cycling. Our results demonstrated that local over-strain of MnO_2 could serve as a gradual failure mechanism, and that by limiting cell DOD strain could be kept reversible throughout the cell.

[a]The CUNY Energy Institute at the City College of New York, Department of Chemical Engineering, Steinman Hall, 160 Convent Ave, New York, NY 10031, USA. E-mail: jgallaway@che.ccny.cuny.edu

[b]Energy Storage Group, Brookhaven National Laboratory, Upton, NY 11973, USA. E-mail: cerdonmez@bnl.gov

[c]Photon Sciences Directorate, Brookhaven National Laboratory, Upton, NY 11973, USA

[d]Department of Physics and Astronomy, Rutgers University, 136 Frelinghuysen Road, Piscataway, NJ 08854, USA

[e]Department of Mechanical and Aerospace Engineering, Princeton University, Princeton, NJ 08544, USA. E-mail: steingart@princeton.edu

[f]Andlinger Center for Energy and the Environment, Princeton University, Princeton, NJ 08544, USA

At low DOD, thousands of cycles can be obtained in specialized alkaline batteries.[8] However, cycle life is generally limited. Our purpose here was to delineate failure mechanisms using mass-produced consumer primary alkaline batteries, which do not differ greatly from specialized cells, although they are not optimized for recharging. Post-mortem analysis of cycled batteries is often a complicated undertaking, as electrode materials can change during disassembly, for example by oxidation, unless extreme care is taken.[9] To complicate matters, the phenomenon initiating failure can trigger secondary effects. For example post-mortem analysis can reveal irreversible material changes in both the anode and cathode, although the processes leading to battery failure likely began in one electrode rather than in both simultaneously. Our hypothesis was that through *in situ* observation we could identify the proximate processes that over time triggered cell failure. Using EDXRD to observe an aged cell cycled *in situ*, we directly observed a ZnO precipitation mechanism that was consistent with a large number of failed cell post mortem analyses.

2. Experimental section

2.1 Consumer primary LR20 cells

The alkaline cells tested were Duracell Duralock MN1300 D cells purchased from Quill Corporation (Lincolnshire, IL). All experiments were performed on batteries from the same package, which was received in September 2012. Specifications were nominally 1.5 V and 15 A h capacity, with an expiration date of Dec 2022. Specific and volumetric energy density were reported as 130 W h kg^{-1} and 322 W h L^{-1}. Deep discharge experiments with these cells resulted in a 0.8 V cutoff capacity of 13.86 A h at 200 mA. Thus 5% was fixed as 0.693 A h.

2.2 Electrochemical cycling

Cell cycling *in situ* during EDXRD was accomplished using a two-channel Arbin BT-5HC. Cells were cycled in a capacity window of 20% DOD or 5% DOD. The sequence of a cycle follows: cell discharge was constant current (CC) to the desired capacity; the cell was held at rest for 30 minutes and charged with a constant-current/constant-voltage (CCCV) profile with a maximum potential of 1.65 V; the cell was again held at rest for 30 minutes and the cycle repeated. In Fig. 2 the minimum current to exit the CCCV step was 60 mA in order to begin a second cycle in the synchrotron beam time allotted. Consequently the discharge capacity shown in Fig. 2 was 2.77 A h, while the charge capacity was 1.97 Ah for a 71% recharge. In Fig. 5 the minimum CCCV current was 20 mA, and charge and discharge capacities were 0.693 Ah, for ~100% coulombic efficiency.

Long term *ex situ* cycling as in Fig. 4 was accomplished using a 32-channel Maccor Model 4600 Battery Test System. *Ex situ* cells were cycled to 5% DOD with a modified CCCV schedule imposing a 15% overcharge on each cycle to account for coulombic inefficiencies during long term cycling. Long-term cell failure was defined as either (1) inability of a cell to accept the charging current or (2) a cycling efficiency below 80% (including the 15% inefficiency imposed by overcharge).

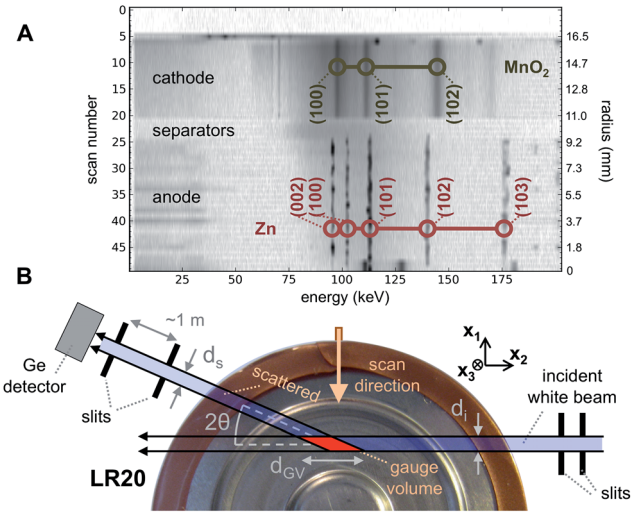

Fig. 1 EDXRD results for an LR20 alkaline Zn–MnO_2 battery. (A) Diffraction contour taken along the radius at battery half-height. Pixel darkness corresponds to the logarithm of scattered X-ray intensity at a constant angle of $2\theta = 3°$. (B) Schematic showing white beam X-ray diffraction from a gauge volume (GV) within the battery at one scan. Red: GV. Blue: scattered beam path. Note that beam and GV sizes are enlarged many fold for visibility.

2.3 Energy dispersive X-ray diffraction (EDXRD)

EDXRD experiments were conducted at the National Synchrotron Light Source (NSLS) on the 7-pole superconducting wiggler beamline X17B1 at Brookhaven National Laboratory (BNL). At 100 keV, this beamline produced a spectral flux per unit solid angle of 3.5×10^{13} photons per s per $mrad^2$/0.1% BW. Incident radiation was white beam radiation with an energy range of 20–200 keV. Scattering of the incident radiation was detected at a fixed angle of $2\theta = 3°$ as a function of scattered radiation energy. The dimensions of the gauge volume (GV) as illustrated in Fig. 1 were defined by the collimation slit settings. Collimation slits were set for values of $d_i = 0.05$ mm and $d_s = 0.1$ mm. Thus in the x_1-direction the GV was 50 μm. The effective GV size in the x_2-direction was $d_{GV} \approx 1.4$ mm.[7] In the x_3-direction the gauge volume was 2 mm. Axially the beam penetrated the cells 35 mm from the cell bottom or negative connection. Material variations in the axial direction were assumed negligible compared to those in the radial direction. Cells were aligned by observing the half point of the onset of scattering on both sides of the cell, while alternatively moving the cell in the x_1 and x_2 directions. Diffracted X-ray intensity *versus* energy was measured with high resolution germanium detector using a digital signal processor and a 8192-channel multichannel analyzer. The channel number to inverse-*d*-spacing and X-ray energy calibration was made using LaB_6 and CeO_2 standards. Experiments in which the cell was spatially oscillated to minimize exposure of the battery active materials to the beam showed no differences with non-oscillated cells. We concluded the beam caused no damage to the battery and all experiments were performed without oscillation.

The white beam flux was sufficient to record diffraction data at any three-dimensional location in the cell. For example, with

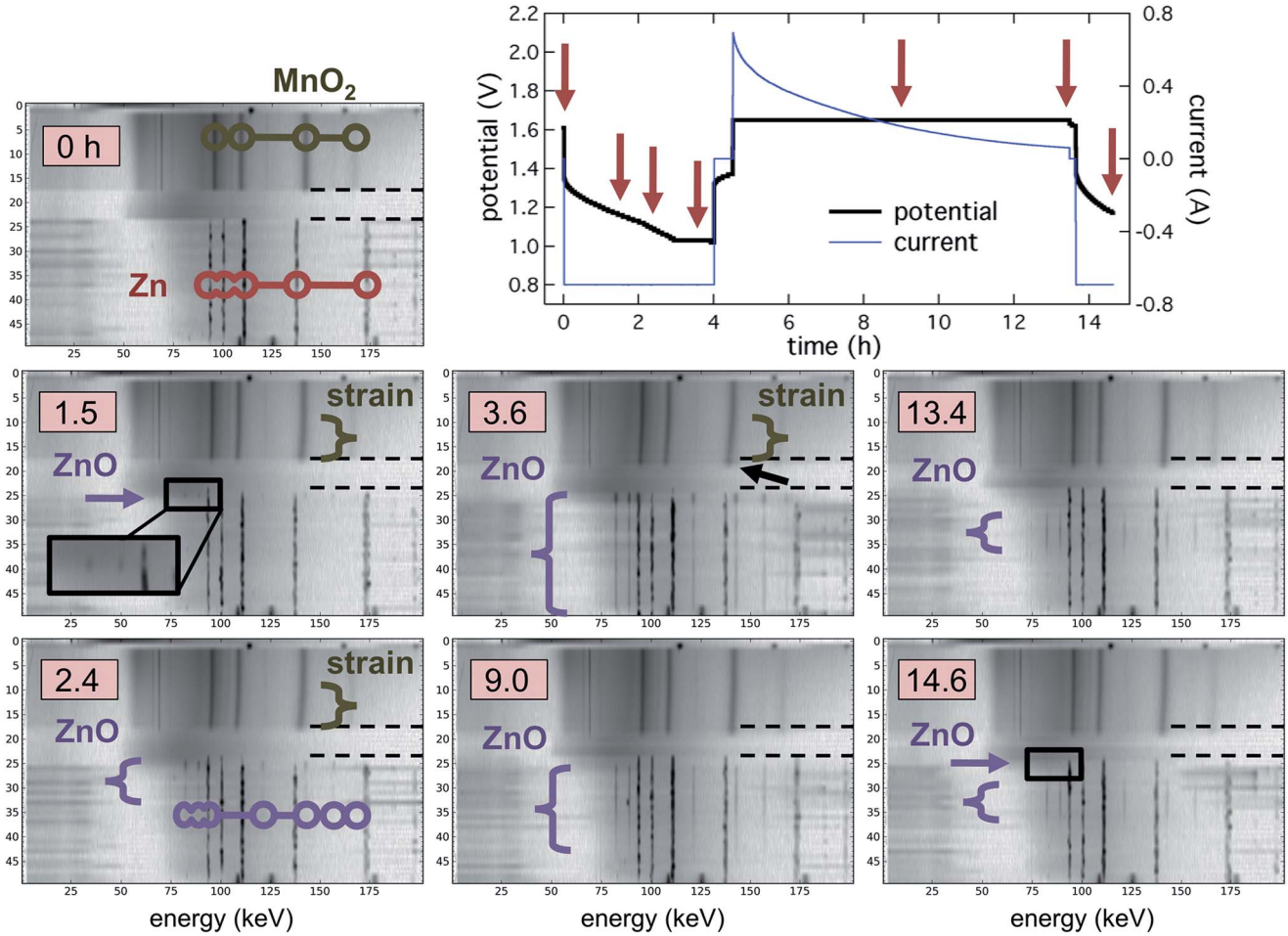

Fig. 2 *In situ* EDXRD of an LR20 alkaline cell discharged to 20% DOD at 0.69 A and CCCV charged with a maximum potential of 1.65 V. Arrows on cell potential/current data indicate diffraction contour timestamps. Violet brackets: zinc oxide profile. Green brackets: MnO_2 lattice strain. Dashed lines: initial location of the separators. Black arrow: cathode expansion.

one second of collection time the detector recorded ~60 000 counts when the GV was positioned at the outer steel can at the top of the cell (see Fig. 1. At this location, the diffracted beam traveled to the detector unobstructed). With the GV positioned at the center of the cell on the battery pin, ~40 000 counts were recorded. Thus attenuation of the beam was not a major effect even at the deepest point in the cell.

2.4 Cell mapping

During *in situ* EDXRD experiments runs were collected continuously, with a run defined as EDXRD data for a full diffraction contour. Cells were mounted on a *x*–*y*–*z* stage and moved while the gauge volume remained fixed in space. All runs began with the beam outside the cell then scanned inward from cathode to anode in the x_1-direction. Each run was broken into 50 scans, with 20 s of data acquisition at each scan. With time for motor motion taken into account, each run was collected in ~19 minutes. LR20 radius was measured to be 16.5 mm. In Fig. 2 this resulted in 340 μm of radius covered per scan. In Fig. 1 and 5 the value was 370 μm per scan, due to a slightly different alignment. Diffraction contour timestamps corresponded to the completion of the last scan in the run. Individual scan data was assigned a more precise timestamp corresponding to the scan in question.

2.5 Scanning electron microscopy (SEM)

Scanning electron micrographs of alkaline cells were collected with a Hitachi TM-3000 benchtop SEM. The SEM images in Fig. 5C are used for illustration only, and are of an LR6 (AA) cell. This cell had the same design principles as an LR20 but was easier to cross-section due to size.

3. Results and discussion

3.1 *In situ* energy dispersive X-ray diffraction (EDXRD)

Using the phase mapping and strain profiling capabilities of EDXRD from a high-energy, high-flux source we examined LR20 batteries as a model for single cells in a large-scale alkaline storage system. This method allowed mapping the cell rapidly with the sealed battery containment intact, as high-energy white beam X-rays penetrated the large battery even at its thickest point of 3.3 cm. In EDXRD, X-rays with a wide range of energies

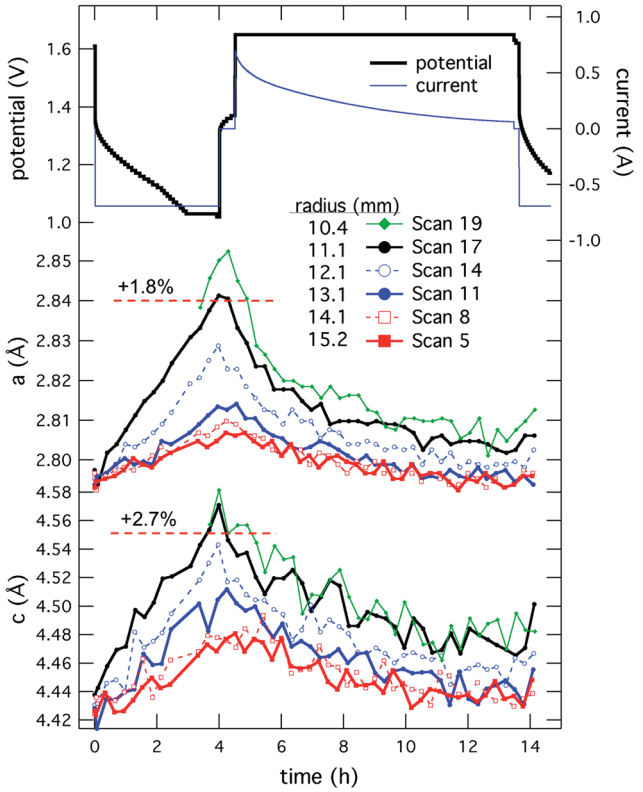

Fig. 3 Calculated ε-MnO_2 lattice parameters *a* and *c* as a function of cell state for the 20% DOD LR20 shown in Fig. 2. Scans were different radii in the cathode, with scan 17 being the initial position closest to the separators (initially $r \approx 10.8$ mm), although the cathode eventually expanded to scan 19 (see Fig. 2). Scan 5 was near the can or cathode current collector ($r \approx 16.2$ mm).

penetrate the cell, and X-ray diffraction intensity is measured at a single angle from a localized gauge volume (GV) within the cell.[10,11] Fig. 1A shows the 1-D radial diffraction contour of an LR20 cell. The *x* and *y* axes respectively show diffracted beam energy and spatial location or scan. Pixel darkness is the logarithm of the diffraction signal. For each scan, the cell was moved, changing the location of the GV inside the cell, as shown in Fig. 1B. Both the cathode active material, ε-MnO_2, and the anode active material, zinc, gave characteristic reflections. Cells had three separators, which caused no reflections: cellophane contacting the cathode, and two fleece separators nearest the anode.

3.2 Effect of depth of discharge in the cathode

A cell cycled in a capacity window of 20% DOD at 0.69 A was monitored continuously by EDXRD, resolving material changes as a function of state of charge. Charging followed a constant-current/constant-voltage (CCCV) protocol. As shown in Fig. 2, material changes in both electrodes were most pronounced at the interface with the separator, as that was the site of highest transfer current.[12] At low DOD, the cathode reaction is a single-phase proton insertion into the manganese dioxide crystal structure.[13–15]

$$MnO_2 + H_2O + e^- = MnOOH + OH^- \quad (1)$$

The increase in ionic radius going from Mn^{4+} to Mn^{3+} results in strain build-up in MnO_2 crystallites. Small values of this strain, associated with shallow discharge, are fully reversible upon proton de-insertion during charging. Irreversibility is correlated with higher lattice strain values attained during discharge.[16] Although the primary causes of this irreversibility remain an area of debate, by observing strain as a function of location in an electrode, irreversibility may be spatially resolved.

During cycling, MnO_2 lattice strains were largest near the separator, causing ε-MnO_2 Bragg lines to shift to lower energy, as indicated in Fig. 2. Between 2.7 and 4 hours (13–20% DOD), the cathode also macroscopically expanded 680 μm (2 scans). Local lattice parameters *a* and *c* for the hexagonal close packed ε-MnO_2 unit cell (space group $P6_3/mmc$) were calculated from the cathode Bragg lines in Fig. 2.[17–20] For each scan Bragg peak maxima were found by fitting each peak to a Gaussian curve. The energy of the peak maximum was converted to *d*-spacing with the beam calibration curve. Miller indices (*hkl*) of the peaks at approximately 96, 112, and 142 keV were (100), (101), and (102) respectively. Using eqn (2) local lattice parameters could be found, and are plotted in Fig. 3.

$$\frac{1}{d^2} = \frac{4}{3}\frac{h^2 + hk + k^2}{a^2} + \frac{l^2}{c^2} \quad (2)$$

In the region closest to the separator, maximum lattice strain was 2.0% in the *a*-direction and 3.2% in the *c*-direction.

Structural irreversibility of EMD during battery cycling is well known. Mondoloni and co-workers reported respective strains of 1.8% in *a* and 2.7% in *c* were associated with onset of structural irreversibility.[16,21] They did this by examining a planar MnO_2/graphite cathode *via in situ* XRD, and found two points of irreversibility. The first point of irreversibility was at 50% conversion to MnOOH at which point lattice strain reached a maximum. The second point of irreversibility was at 80% conversion to MnOOH and resulted in more rapid deterioration of the cathode. In the work by Mondoloni *et al.* the cathode was treated as a steady-state whole, without the capability of resolving the cathode spatially as can be done using EDXRD. This second point of irreversibility corresponded to that reported by Kordesch in 1981, who stated that reversibility was poor if the electrode was cycled beyond an averaged state of $MnO_{1.6}$.[5,22]

In Fig. 3, strains equal to those reported irreversible by Mondoloni occurred at 3.3 hours, or an average DOD of 16.5%. As the current distribution was not uniform, lattice strain could be used to estimate local DOD in the cathode. While this cell was discharging to 20% of measured cell capacity, at this rate the cathode active material within 680 μm of the separator was discharging over 50% 1-electron capacity, and was thus partially irreversible. There was observable lattice strain near the current collector as well, although it was far less pronounced: only 0.4% in the *a*-direction. The results in Fig. 3 indicated that for a cathode of this thickness, porosity and conductivity, this cycling protocol resulted in partial irreversibility of MnO_2 in a 680 μm region adjacent to the separator. Over many cycles, we expected

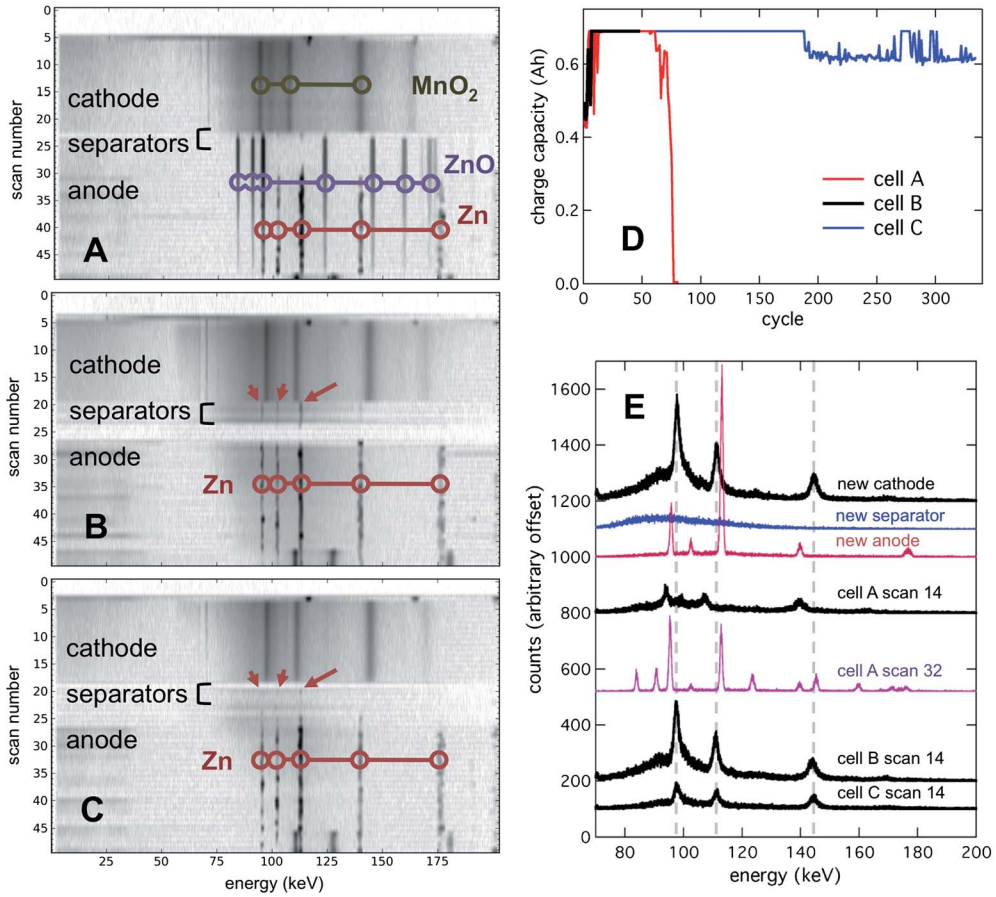

Fig. 4 Ex situ EDXRD analysis of alkaline cells cycled at 5% DOD. Brackets show the location of the three separators in new cells. (A) Post-mortem EDXRD of a cell that failed at 72 cycles due to a high cell impedance. ZnO was found throughout the separators and in the anode. (B) A cell halted at the top of its cycling window that was cycling with good efficiency at 48 cycles. Maroon arrows show zinc reflections in the separators. This was the cell cycled *in situ* in Fig. 5. (C) A cell halted with good efficiency at 334 cycles. (D) Charge capacities of the cells in (A–C). (E) Individual scan data compared to those in new cells. Dashed lines: MnO_2 peak energies in a new cathode.

this to result in capacity fade as MnO_2 was gradually rendered irreversible.

Thus MnO_2 over-strain would serve as a failure mechanism during 20% DOD cycling. A second cell was cycled at the same rate to only 5% DOD, well away from the DOD value of 16.5% observed to cause irreversible strain. Cycling at 5% DOD, maximum local strain values were only 0.4% and 1.3% in the *a*- and *c*-directions, indicating strain remained reversible throughout the cathode in this cell.

Although zinc anodes have high electrical conductivity, electrolyte resistance results in a current distribution localized within a penetration zone near the separator.[23] In the anode of the cell discharged to 20% DOD, zinc was electrochemically converted to zincate by reaction [3], causing zinc reflections to fade at the separator interface.[24]

$$Zn + 4OH^- = Zn(OH)_4^{2-} + 2e^- \quad (3)$$

The solubility of zincate depends on electrolyte pH, and zincate will precipitate as zinc oxide *via* reaction [4] if its concentration is above the solubility limit.

$$Zn(OH)_4^{2-} = ZnO + 2OH^- + H_2O \quad (4)$$

In Fig. 2, zinc oxide reflections were first observed at the anode–separator interface at 7.5% DOD (1.5 hours into discharge). This substantial interfacial ZnO layer grew to 1.1 mm thickness during discharge. ZnO also spread throughout the anode at a lower intensity (~14% of that in the interfacial layer), likely indicating Zn–ZnO core–shell formations.[25,26] ZnO did not precipitate in the separators at any detectable level. During CCCV charging, ZnO re-dissolved in the interfacial layer and zinc was deposited in its place. The ZnO distributed across the anode thickness re-dissolved in dual fronts propagating inwards from the separators and the current collector. This resulted in a zone of ZnO in the electrode middle as the recharge in Fig. 2 was left incomplete due to time constraints. Despite this, the material evolution in the anode appeared to be fully reversible judged by EDXRD results of one cycle. ZnO has previously been detected in discharged electrodes at levels above a volume fraction of ~0.1 in the anode.[25] However these and similar methods have relied on destructive, *ex situ* techniques.

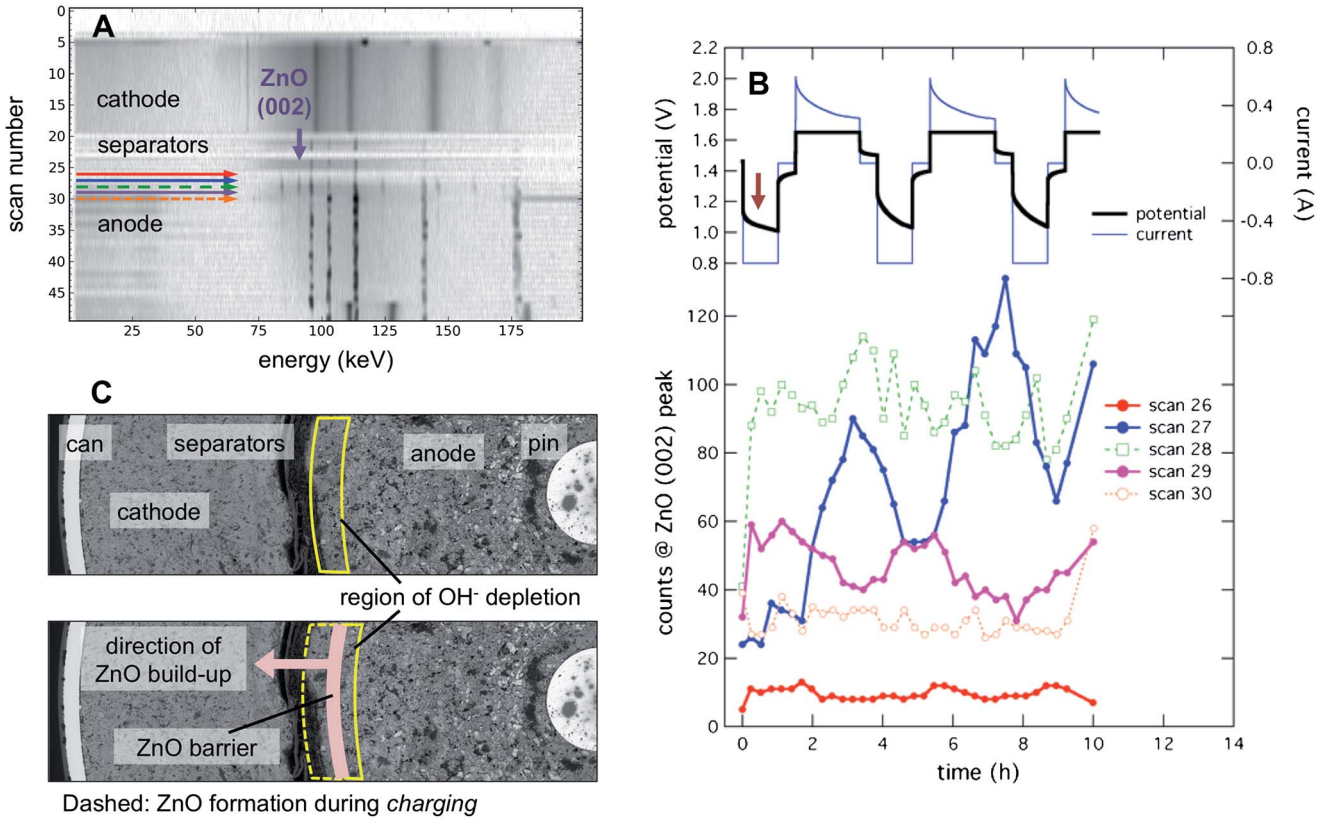

Fig. 5 ZnO build-up in an LR20 cell aged 48 cycles at 5% DOD. (A) Diffraction contour just after beginning the cycle 49 discharge, revealing an evolving ZnO layer near the separator. This layer formed suddenly. Horizontal arrows: scan locations plotted in panel B. (B) *In situ* cycling data correlated with intensity of the (002) ZnO reflection at five radii near the separator. Note ZnO build-up at scan 27. Maroon arrow: timestamp of the contour in panel A. (C) Illustration of ZnO build-up caused by a ZnO blocking layer.

3.3 Long-term cycling at limited depth of discharge

The above results indicate cells cycled at 5% DOD would be unaffected by over-strain of the cathode active material. An experimental group of LR20 cells were cycled at 5% DOD to obtain a profile of cell failure modes and correlate these with post-mortem EDXRD results. Among cells that failed, which were tested after failure in the cycle range 72–411: 13% of failures were due to containment failure of the battery seal; 7% were due to a low cell impedance, which we attributed to dendrites; and 80% were due to a high cell impedance, which prevented the cell from accepting charging current. As a control group, several cells were halted while cycling at good efficiency at the top of their charging window. The cycle range of the control group was 48–334.

Fig. 4A shows post-mortem EDXRD results for a typical cell that displayed the high impedance failure mode at cycle 72. Fig. 4B and C show typical control cells halted with good efficiency at cycles 48 and 334 respectively. Fig. 4D compares the charge capacities for each of these cells. Fig. 4E compares representative scans from the three cells to those in a new cell. The cell failed by high impedance had substantial material changes throughout the cell: the cathode MnO_2 peaks were shifted with respect to the control corresponding to 4% strain; the separator was saturated with ZnO; and ZnO was found throughout the anode. The presence of ZnO in the separator and anode was common to all high impedance cells. Cathodes in high impedance cells were found either unstrained, strained, or with additional MnO_x phases, with all cases accompanied by extensive ZnO formation. In contrast, no control cell halted with good efficiency had detectable ZnO anywhere in the cell. This suggests that persistent ZnO does not build up slowly in cells cycling with good efficiency. However, all control cells did show zinc infiltration into the separator area, indicated by maroon arrows in Fig. 4. As few cells failed due to dendrites, this indicated the cellophane separator effectively contained dendrites in this cycle range. MnO_2 crystallinity decreased steadily in control cells during cycling, although strain was minimal and this did not appear to trigger failure.

3.4 *In situ* cycling of a cell aged at limited depth of discharge

The long term cycling results raised two questions: (1) what material change was the proximate cause of cell failure in high impedance cells if EDXRD revealed changes in both electrodes, and (2) by what mechanism does ZnO form in a cell separator if it cannot be detected building up in control cells which have reached considerable cycle life with good efficiency?

To observe *in situ* performance of a cell at advanced cycle numbers, a cell aged for 48 cycles was halted, transported to

BNL, and cycling was resumed while performing *in situ* EDXRD. Initially no ZnO was observed in the cell (Fig. 4B). Upon beginning cycle 49 a blocking layer of ZnO formed at the separator–anode interface, shown in Fig. 5A. Three cycles were observed *in situ*, and this ZnO blocking layer remained persistent and was not reversed during charging. Intensity of the ZnO (002) reflection at the blocking layer location (scan 28) showed no correlation with the cell state of charge, shown in Fig. 5B. Furthermore, this blocking layer caused a steady build-up of ZnO in the direction of the separators at scan 27. Significantly, the relationship there between ZnO formation and state of charge was opposite that expected in the bulk of the anode. At scan 27 ZnO steadily formed during charge cycles (*cf.* scan 29, where ZnO formed during discharge as expected), and was only partially unformed during discharge. With every cycle ZnO intensity there increased ~40%. This demonstrated how ZnO can irreversibly precipitate, build up, and reach the separators.

Once a ZnO blocking layer has formed, the mechanism of ZnO build-up in the separator direction is straightforward to explain. In the range 0–14 M KOH, zincate solubility decreases monotonically with decreasing KOH concentration.[27] Modeling studies by Chen and Cheh indicate that in the starved electrolyte environment within an alkaline cell, local concentration of OH^- varies widely during cycling, and flux of OH^- is dominated by electrical migration.[28,29] Podlaha and Cheh, modeling a LR6 cell, showed that net flux at the separator–anode interface is expected to result in local OH^- depletion during discharge.[30,31] While OH^- is produced in the cathode during discharge, the barrier presented by the separator results in a lower OH^- flux from the cathode than that toward the anode current collector. A lower OH^- concentration (*i.e.* lower pH) shifts the equilibrium of eqn (4) and results in ZnO precipitation locally at this interface. In our cell, the ZnO blocking layer at scan 28 presented a sufficient barrier to OH^- flux to shift the location of greatest OH^- depletion during discharge to scan 29, illustrated in Fig. 5C. Conversely, at scan 27, OH^- flux from the cathode during discharge was greater than that through the ZnO layer and toward the anode current collector. This caused ZnO at scan 27 to dissolve during discharge and precipitate during charge.

We hypothesize this mechanism can lead to ZnO precipitation in the separator, causing high cell impedance and initiating failure. In specialized cells cycled somewhat deeper than those described here, a black, non-porous ZnO crust has been reported between the anode and separator.[32] Shen and Kordesch hypothesized this layer formation was the consequence of gradual ZnO deposition over many cycles. In the results reported here, we could not detect ZnO in any cells halted during cycling, regardless of cycle number. Thus we conclude that while the ZnO build-up illustrated in Fig. 5 does occur over a few cycles, it is otherwise rapid, and not the result of a steady or gradual process.

This leaves the question of how the ZnO blocking layer formed, leading to ZnO build-up. The formation was not gradual, but was a contingent or triggered phenomenon. As this cell had been halted and re-started for *in situ* cycling, the extended (~24 hour) rest period may be involved. Realistic battery duty cycles are expected to involve periods of rest such as this, and therefore understanding of how they can trigger otherwise unlikely material changes is critical for large-scale battery deployment. ZnO formation in alkaline batteries is not a completely understood phenomenon. Model systems have shown that formation of passivating ZnO films during electrode discharge proceeds through a complicated mechanism of ZnO precipitation, aggregation, networking, and crystallization, and not through a solid state reaction.[33] *In situ* X-ray microtomography has shown zinc dissolution and ZnO formation preferentially at the separator interface, with particle size changing only slightly elsewhere in the electrode.[34,35]

4. Conclusions

In contrast to other *in situ* visualization techniques, EDXRD at high flux and high energy from a superconducting wiggler allowed rapid data collection and therefore realistic battery cycling rates. The ability to define a GV in space and position it inside the cell enabled material information to be collected as a function of position with high resolution. We have used EDXRD to identify materials changes associated with alkaline battery failure mechanisms, occurring in both electrodes, as a function of DOD and cycle number. In the cathode over-strain of MnO_2 was observed at 16.5% DOD. This over-strain was localized near the separator, and it was expected this would result in gradual degradation and failure of the cathode during extended cycling. During cycling limited to 5% DOD, no cathode over-strain was detected. However, localized ZnO precipitation in the anode was observed. This ZnO precipitation was consistent with the post-mortem analyses of a number of failed cells, suggesting that at 5% DOD ZnO may frequently be responsible for initiating failure. By visualizing localized irreversibilities within alkaline cells, methods can be developed for cycling them to enable the use of these safe, abundant, and inexpensive materials for large scale electrical storage.

Acknowledgements

This work was supported by the Laboratory Directed Research and Development Program of Brookhaven National Laboratory (LDRD-BNL) under contract no. DE-AC02-98CH 10866 with the U.S. Department of Energy. Zn–MnO_2 research at the CUNY Energy Institute was funded in part by the Advanced Research Projects Agency – Energy (ARPA-E), U.S. Department of Energy, under Award Number DE-AR0000150. Use of the National Synchrotron Light Source, Brookhaven National Laboratory, was supported by the U.S. Department of Energy, Office of Science, Office of Basic Energy Sciences, under contract no. DE-AC02-98CH10886.

References and Notes

1 M. Armand and J. M. Tarascon, *Nature*, 2008, **451**, 652–657.
2 B. Dunn, H. Kamath and J. M. Tarascon, *Science*, 2011, **334**, 928–935.

3 Z. Yang, J. Zhang, M. C. W. Kintner-Meyer, X. Lu, D. Choi, J. P. Lemmon and J. Liu, *Chem. Rev.*, 2011, **111**, 3577–3613.
4 K. Kordesch, J. Gsellman and K. Tomantschger, *J. Electroanal. Chem.*, 1981, **118**, 187–201.
5 K. Kordesch, J. Gsellmann, M. Peri, K. Tomantschger and R. Chemelli, *Electrochim. Acta*, 1981, **26**, 1495–1504.
6 R. Patrice, B. Gerand, J. B. Leriche, L. Seguin, E. Wang, R. Moses, K. Brandt and J. M. Tarascon, *J. Electrochem. Soc.*, 2001, **148**, A448–A455.
7 M. Croft, I. Zakharchenko, Z. Zhong, Y. Gurlak, J. Hastings, J. Hu, R. Holtz, M. DaSilva and T. Tsakalakos, *J. Appl. Phys.*, 2002, **92**, 578–586.
8 J. Daniel-Ivad, in *Encyclopedia of Electrochemical Power Sources*, ed. J. Garche, C. Dyer, P. Moseley, Z. Ogumi, D. Rand and B. Scrosati, Elsevier, Amsterdam, 2009, vol. 5, pp. 497–512.
9 D. Aurbach, B. Markovsky, A. Rodkin, M. Cojocaru, E. Levi and H. J. Kim, *Electrochim. Acta*, 2002, **47**, 1899–1911.
10 J. Rijssenbeek, Y. Gao, Z. Zhong, M. Croft, N. Jisrawi, A. Ignatov and T. Tsakalakos, *J. Power Sources*, 2011, **196**, 2332–2339.
11 E. S. Takeuchi, A. C. Marschilok, K. J. Takeuchi, A. Ignatov, Z. Zhong and M. Croft, *Energy Environ. Sci.*, 2013, **6**, 1465–1470.
12 J. S. Newman and C. W. Tobias, *J. Electrochem. Soc.*, 1962, **109**, C193.
13 A. Kozawa and R. A. Powers, *J. Electrochem. Soc.*, 1966, **113**, 870–878.
14 A. Kozawa and R. A. Powers, *J. Electrochem. Soc.*, 1968, **115**, 122–126.
15 S. W. Donne, G. A. Lawrance and D. A. J. Swinkels, *J. Electrochem. Soc.*, 1997, **144**, 2954–2961.
16 C. Mondoloni, M. Laborde, J. Rioux, E. Andoni and C. Levyclement, *J. Electrochem. Soc.*, 1992, **139**, 954–959.
17 C. H. Kim, Z. Akase, L. C. Zhang, A. H. Heuer, A. E. Newman and P. J. Hughes, *J. Solid State Chem.*, 2006, **179**, 753–774.
18 W. Bowden, R. Sirotina and S. Hackney, *ITE Lett. Batteries, New Technol. Med.*, 2003, **4**, B1.
19 Y. Chabre and J. Pannetier, *Prog. Solid State Chem.*, 1995, **23**, 1–130.
20 D. E. Simon, R. W. Morton and J. J. Gislason, *Adv. X-Ray Anal.*, 2004, **47**, 267–280.
21 In the work of Mondoloni, the peaks assigned to γ-MnO2 were used to calculate lattice parameters assuming an orthorhombic unit cell. For this reason our values for a and c were switched compared to theirs. There is some controversy over the structure of EMD, for example see ref. 17–20 for ε-MnO2 and γ-MnO2 hypotheses. We assumed the comparison of lattice parameter values was valid, as unit cell strain was a function of manganese atom ionic radius in both cases.
22 This notation was meant to signify the average oxidation state of the manganese atoms in the lattice. Thus $MnO_{1.5}$ ideally corresponds to MnOOH, and $MnO_{1.6}$ indicates 80% totalconversion of MnO_2 to MnOOH.
23 M. B. Liu, G. M. Cook and N. P. Yao, *J. Electrochem. Soc.*, 1982, **129**, 239–246.
24 F. R. McLarnon and E. J. Cairns, *J. Electrochem. Soc.*, 1991, **138**, 645–664.
25 W. G. Sunu and D. N. Bennion, *J. Electrochem. Soc.*, 1980, **127**, 2017–2025.
26 Q. C. Horn and Y. Shao-Horn, *J. Electrochem. Soc.*, 2003, **150**, A652–A658.
27 W. H. Dyson, L. A. Schreier, W. P. Sholette and A. J. Salkind, *J. Electrochem. Soc.*, 1968, **115**, 566–569.
28 J. S. Chen and H. Y. Cheh, *J. Electrochem. Soc.*, 1993, **140**, 1205–1213.
29 J. S. Chen and H. Y. Cheh, *J. Electrochem. Soc.*, 1993, **140**, 1213–1218.
30 E. J. Podlaha and H. Y. Cheh, *J. Electrochem. Soc.*, 1994, **141**, 15–27.
31 E. J. Podlaha and H. Y. Cheh, *J. Electrochem. Soc.*, 1994, **141**, 28–35.
32 Y. W. Shen and K. Kordesch, *J. Power Sources*, 2000, **87**, 162–166.
33 I. Arise, S. Kawai, Y. Fukunaka and F. R. McLarnon, *J. Electrochem. Soc.*, 2013, **160**, D66–D74.
34 A. Haibel, I. Manke, A. Melzer and J. Banhart, *J. Electrochem. Soc.*, 2010, **157**, A387–A391.
35 I. Manke, H. Markotter, C. Totzke, N. Kardjilov, R. Grothausmann, M. Dawson, C. Hartnig, S. Haas, D. Thomas, A. Hoell, C. Genzel and J. Banhart, *Adv. Eng. Mater.*, 2011, **13**, 712–729.

